ADVANCED MATERIALS
www.advmat.de

Inverted Colloidal Quantum Dot Solar Cells

Gi-Hwan Kim, Bright Walker, Hak-Beom Kim, Jin Young Kim, Edward H. Sargent, Jongnam Park,* and Jin Young Kim**

Colloidal quantum dot (CQD) solar cells have emerged as a promising class of solar cell with the potential to be manufactured at low cost.[1] PbS CQDs in particular are readily synthesized from earth-abundant elements,[2,3] and their bandgap can be conveniently and widely tuned via control over nanoparticle size.[4] Efficient, air-stable solar cells can be fabricated under ambient conditions using solution processing techniques.[5] PbS CQDs can behave either as a p-type or n-type semiconductors,[6] allowing their use in a wide variety of architectures including hybrid organic/inorganic devices.[7] These materials absorb light at wavelengths of 1100 nm and beyond, offering the potential for large photocurrents compared to many widely-employed organic and inorganic materials. Additionally, CQD solar cells offer routes to efficiencies exceeding the Shockley-Queisser limit for solar cells[8,9] via their ability to exploit multiple excitons,[10,11] their promise in hot carrier extraction,[12] and their enablement of size-tuned tandem and multijunction cells. Recent advances in the understanding of CQD solar cells and device fabrication have led to the demonstration of quantum efficiencies over 100%,[10,11] and increases in certified power conversion efficiency (PCE) to 7%.[13–15]

The PCE of a CQD solar cell is directly proportional to the generated photocurrent, which is determined primarily by the fraction of incident photons absorbed in the CQD layer and by the number of extracted carriers per absorbed photon. A CQD film thickness of~1 μm is typically required to absorb all incident photons, but such thick films are often accompanied by insufficient charge transport for complete carrier extraction, limiting the optimal layer thickness to~300 nm or less and thus reducing the amount of light absorbed by the CQD layer. Also, in the device structure widely-employed in prior CQD solar reports (here referred to as "standard"), the PbS CQD layer is located immediately adjacent the reflective metal electrode. As a result, the intensity of the optical field responsible for charge carrier generation in the CQD layer drops to near-zero proximate to the metal interface.[16,17] This further reduces the amount of light that can be absorbed by the PbS layer, and limits degrees of freedom in engineering maximal absorption within a given thickness of CQD material.

To address these issues, it is attractive to architect the CQD solar cell so that more light is absorbed by an active layer of limited thickness, enabling avenues to enhanced PCE. In this work, we build a solar cell that is inverted in architecture compared to the standard, previously-reported, CQD photovoltaic device. This enables us to explore the introduction and engineering of an optical cavity for light enhancement. Specifically, we insert an optical spacer in a CQD photovoltaic device in order to enhance PCE by tuning the spatial distribution of the optical field.[18,19]

A materials advance is pursued, achieved, and explained in the present work that is crucial to the realization of the inverted, optically-tuned, architecture. We employ a substantially transparent ZnO optical spacer between the photoactive CQD layer and the reflective metal electrode in an inverted device configuration. To do so, we develop the means to integrate a low-temperature, solution-processed, n-type ZnO layer as an optical spacer atop the CQD absorber. We show that the spacer offers significant prospects for enhancing light absorption in the CQD layer since careful choice of ZnO thickness enables judicious placement of the optical field maxima within the absorber by optical simulations. Moreover, we demonstrate by experiments that the light harvesting and the photovoltaic efficiency can be significantly improved in CQD solar cells by tuning the thickness of the active layer and inserting an optical spacer between the active layer and the reflective electrode.

As discussed herein, the new architecture offers an improvement in performance relative to the reference device that goes beyond optical cavity enhancement alone. We investigate using ultraviolet photoemission spectroscopy the detailed electronic structure of each of the materials incorporated into the materials stack in each case. In this way, we offer experimentally-substantiated spatial band diagrams of the device that detail the origins of the enhanced voltage in the device.

Figure 1 shows the device structures studied in this work. The devices were fabricated on indium tin oxide (ITO) coated substrates and all processing steps, except a brief immersion in a 3-mercaptopropionic acid (MPA) solution and the final metal electrode deposition, were performed by spin-coating in air. The ZnO optical spacer was prepared using a diethyl zinc precursor and deposited on the CQD layer. The reactive diethyl zinc precursor decomposes rapidly to form ZnO in the presence of air and only mild thermal annealing (110 °C) is required to prepare the film via this route. The low processing temperature of the ZnO layer is critical to the success of the inverted architecture; other methods of ZnO preparation which

G.-H. Kim, Dr. B. Walker, H.-B. Kim, Prof. J. Park, Prof. J. Y. Kim
Interdisciplinary School of Green Energy
Ulsan National Institute of Science and Technology (UNIST)
Ulsan 689–798, South Korea
E-mail: jnpark@unist.ac.kr; jykim@unist.ac.kr
Dr. J. Y. Kim, Prof. E. H. Sargent
Electrical and Computer Engineering
University of Toronto
10 King's College Rd, Toronto ON, Canada M5S 3G4
E-mail: ted.sargent@utoronto.ca
Dr. J. Y. Kim
Fuel Cell Research Center
Korea Institute of Science and Technology
Seoul 136-791, South Korea

DOI: 10.1002/adma.201305583

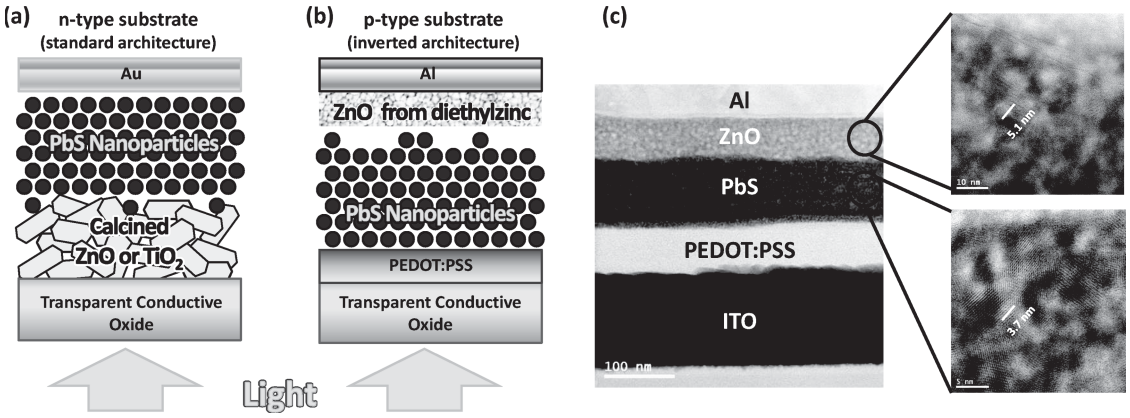

Figure 1. Schematic diagram comparing depleted heterojunction architectures using (a) n-type substrate and (b) p-type substrate. (c) High resolution-transmission electron microscopy (HR-TEM) cross-sectional image of p-type substrate cells (magnified PbS and ZnO regions).

require high processing temperatures will destroy the quantum confinement and electronic properties of the PbS CQD layer. To investigate the effect of the optical cavity in the photovoltaic device structure, we fabricated heterojunction devices structure composed of ZnO and PbS CQD layers with an inverted configuration using Poly(3,4-ethylenedioxythiophene):poly(4-styrenesulfonate) (PEDOT:PSS) as a hole-transporting layer. For comparison, prior to the insertion of ZnO optical spacer, we also optimized standard solar cell structures. Figures 1a and b schematically depict the studied standard and inverted structure devices.

We sought to investigate the energy band structure of the PbS CQD and ZnO layers from an electronic materials perspective. To this end, ultraviolet photoelectron spectra (see **Figure 2**) were collected for each material. Fermi energies (E_F) were determined from the secondary edge region and found to be 4.2 and 5.0 eV, respectively, for the ZnO and PbS CQD films. The energy of the valence band edge (E_{VB}) of the ZnO layer was obtained from the low binding energy onset relative to an Au reference and was found to be 7.3 eV. The absorption onset of the ZnO layer was observed at 370 nm, indicating an optical bandgap (E_g) of 3.4 eV. Subtracting the optical bandgap from the valence band energy yields an estimation of the conduction band energy (E_{CB}) of 3.9 eV. E_g, E_{VB} and E_{CB} were found for the PbS CQD film using the analogous methods, and determined to be 1.2, 5.1 and 3.9 eV, respectively, consistent with previously reported values for PbS CQD films.[4] Energy band diagrams based on this data can be found in Figure 2.

The band structure of the junction indicates that separation of photogenerated charge carriers is favored at the PbS CQD/ZnO interface. Electrons drift through the PbS CQD layer to the ZnO layer and are collected at the aluminum cathode, while holes drift through the PEDOT:PSS layer to be collected at the ITO electrode.

Figure 1c shows cross-sectional high resolution transmission electron microscope (HR-TEM) images of the inverted device architecture. A magnified image of the PbS CQD layer reveals regularly ordered atomic structures with crystalline domains of about 3.7 nm, consistent with absorption onset (~950 nm, see Figure S1). Crystalline domains of about 5.1 nm are observed in the ZnO layer. The surface morphologies of the ZnO and PbS CQD layers were characterized by atomic force microscopy. ZnO films were as uniform and conformal layers where the surface roughness depends strongly on the smoothness of underlying layer: the ZnO films showed an RMS roughness of 1.9 nm and 3.8 nm when deposited on ITO substrates and PbS CQD films, respectively. Spin-cast PbS CQD films, which were deposited using a solid-state ligand exchange process using MPA as a cross-linking agent, showed somewhat rougher surface morphologies, with an RMS roughness of 4.7 and 4.2 nm for films prepared on ZnO and PEDOT:PSS substrates, respectively (see Figure S2).

In order to gain insight into the operation of the optical spacer layer in light harvesting and the photocurrent generated in the device structures, we first estimated photocurrent generation by calculating the amount of light absorbed in the active layer in devices with variable CQD film and ZnO thicknesses. We constructed optical models based on a transfer matrix formalism introduced by Burkhard et al.[18] to calculate the fraction of light absorbed at different wavelengths within the CQD film in the device structure. Optical constants (n and κ, the real and imaginary parts of the index of refraction) and thicknesses of the various layers in the device constitute the inputs into this model. The optical constants of each layer were measured using ellipsometry (Figure S3). In the case of PbS CQD films, κ values were derived from the absorption coefficient (α) of PbS CQD films via the equation $\kappa = 4\pi\alpha\lambda^{-1}$, while n values were approximated based on the known refractive index of bulk PbS assuming a nanocomposite consisting of close-packed PbS spheres (a volume fraction of $\pi/(3\sqrt{2})$ or 74 volume%) in a manner similar to that previously used to model Bi_2S_3 nanocrystal films.[20] It is likely that this approximation slightly overestimates the refractive index of PbS film as the nanoparticles do not form a perfect close-packed structure and part of the volume includes the organic cross-linker MPA. We evaluate sensitivity of the model to these perturbations in Figure S4. Then, to calculate maximum generated photocurrent within the device, we assumed that photogenerated charge carriers produced by absorption in the PbS CQD layer results in extraction with high internal quantum efficiency as long as the CQD is thinner than about 300 nm. Based on this approximation, we were able to estimate the

Adv. Mater. 2014,
DOI: 10.1002/adma.201305583

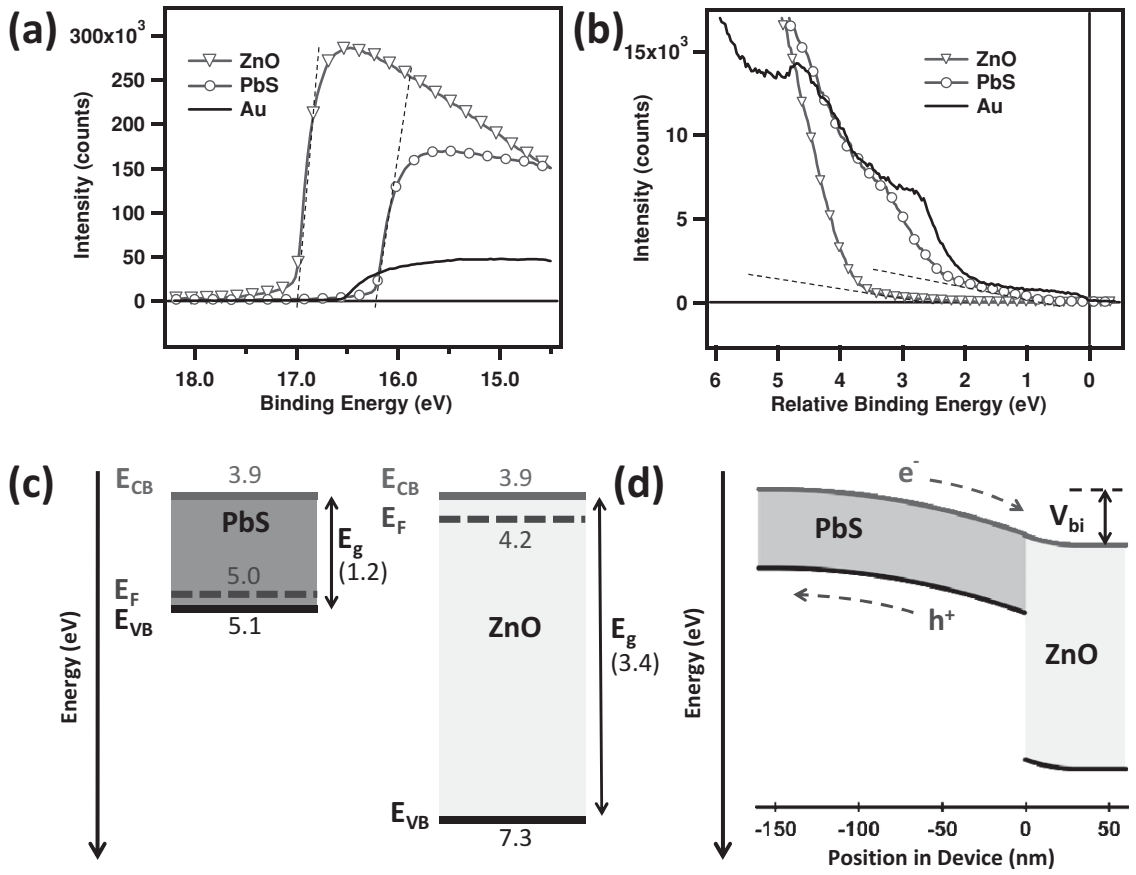

Figure 2. Electronic properties of ZnO and PbS films. (a) Secondary edge region of ultraviolet photoelectron spectra (UPS) of PbS and ZnO compared to an Au reference. (b) Low energy onset region of UPS spectra of PbS and ZnO plotted relative to an Au reference. (c) Energy level diagrams showing conduction band (E_{CB}), valence band (E_{VB}) and Fermi energies (E_F) of ZnO and PbS films derived from UPS data. (d) Band diagram depicting the depleted PbS/ZnO heterojunction.

photocurrent generation capability of the studied device architectures.

Figure 3 shows a plot of the calculated short-circuit current density (J_{SC}) for the both device structures as a function of ZnO and PbS CQD layer thicknesses; Figure S5 compares the difference of photocurrent performance generated within two device structures. We see that for thin PbS layers, incorporating a ZnO optical spacer between the PbS CQD absorber and reflective electrode can dramatically increase the J_{SC}. For example, for 10 nm thickness of the PbS CQD film and 45 nm

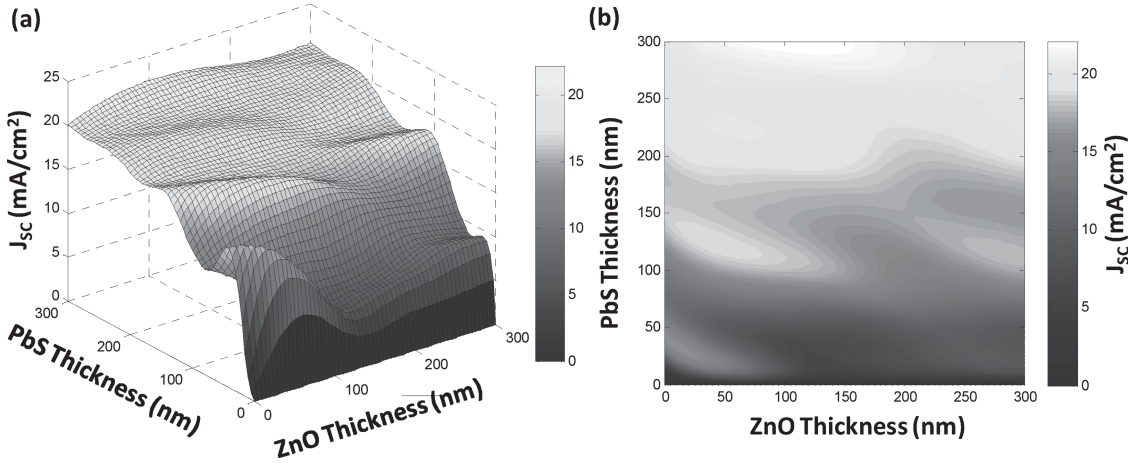

Figure 3. Simulated short circuit current density as a function of ZnO and PbS layer thicknesses obtained via transfer matrix modeling of the inverted (ITO/PEDOT:PSS/PbS/ZnO/Al) structure, plotted (a) in 3-dimensions and (b) as a contour map.

thickness of the ZnO, the J_{SC} reaches a higher value of 11.6 mA/cm^2 in the inverted configuration than in the standard structure, which shows a J_{SC} of 5.9 mA/cm^2. At 95 nm thickness of PbS and 70 nm of ZnO, we also observed a similar trend: the J_{SC} increases from 15.3 mA/cm^2 to 19.7 mA/cm^2 when applied to inverted structure. However, as the influence of an optical spacer on the photocurrents generated within the PbS CQD layer is coupled to the thickness and optical properties of all the other layers in the device, we noticed it is also possible to produce a reduced photocurrent with the optical spacer ZnO layer. This result suggests that the use of an optical spacer in CQD solar cells may benefit photocurrent due to the optical cavity effect, when the constructive interference effects caused by the inserted optical spacer are distributed within the CQD layers. Additionally, the constructive interference effect caused by ZnO becomes smaller for thicker PbS CQD layers as the PbS CQD films absorb a greater fraction of light in the first pass, while reflected light plays a less significant role. The threshold into this regime occurs when all above-bandgap solar light is substantially absorbed in a single pass, i.e. when the absorber thickness > $1/\alpha$.

We proceeded to test experimentally the optical spacer effect for the studied photovoltaic device architectures to challenge the relationship of modeling results to experimental device characteristics. For the study, we constructed a suite of standard (ITO/ZnO/PbS/Au) and inverted (ITO/PEDOT:PSS/PbS/ZnO/Al) photovoltaic devices with various thicknesses of PbS CQD and ZnO layers. Here, the thickness of the active layer was optimized based on the results of the best performing devices derived from optical modeling study. The same materials and procedures were used to prepare the PbS and ZnO layers in both architectures. Although the difference in Fermi energies (~0.8 eV) between the PbS CQD and ZnO layers should provide the same built-in potential for either the standard or inverted architecture, the position change of the PbS CQD (p-type) and ZnO (n-type) layers changes the type of charge carrier collected at the substrate and reflective top electrodes. Therefore, it is necessary to change the electrode materials in order to accommodate this change in polarity. High work function (ϕ = 5.0 eV) Au top electrodes were used in the standard architecture in order to lower the Fermi energy at the anode and facilitate the collection of holes, while low work function (ϕ = 4.2 eV) Al top electrodes were used for the inverted architecture in order to increase the Fermi energy at the cathode and facilitate the collection of electrons. Additionally, a PEDOT:PSS layer (ϕ = 5.2 eV) was used on top of the ITO substrate (ϕ = 4.5 eV) to increase the work function of the substrate and prevent the formation of micro-shorts through defects in the PbS CQD layer, as a high failure rate and low PCE (1.1%) were observed in inverted devices without PEDOT:PSS layers.

To characterize the effect of ZnO optical spacer layer on the photovoltaic properties of the device, we examined the current density-voltage (*J–V*) behavior in the cells with various thicknesses of the layers with and without optical spacer (**Figure 4** and Figure S6) and their performance parameters are listed in **Table 1** and **2**. The experimental results generally support the enhanced photocurrent values upon insertion of an optical spacer, as expected from the modeling results. Under optimized device fabrication conditions, the J_{SC} increases from 9.9 mA/cm^2 to 13.5 mA/cm^2 without and with an optical spacer, respectively. Hence, the PCE increases from 2.5% to 4.3%.

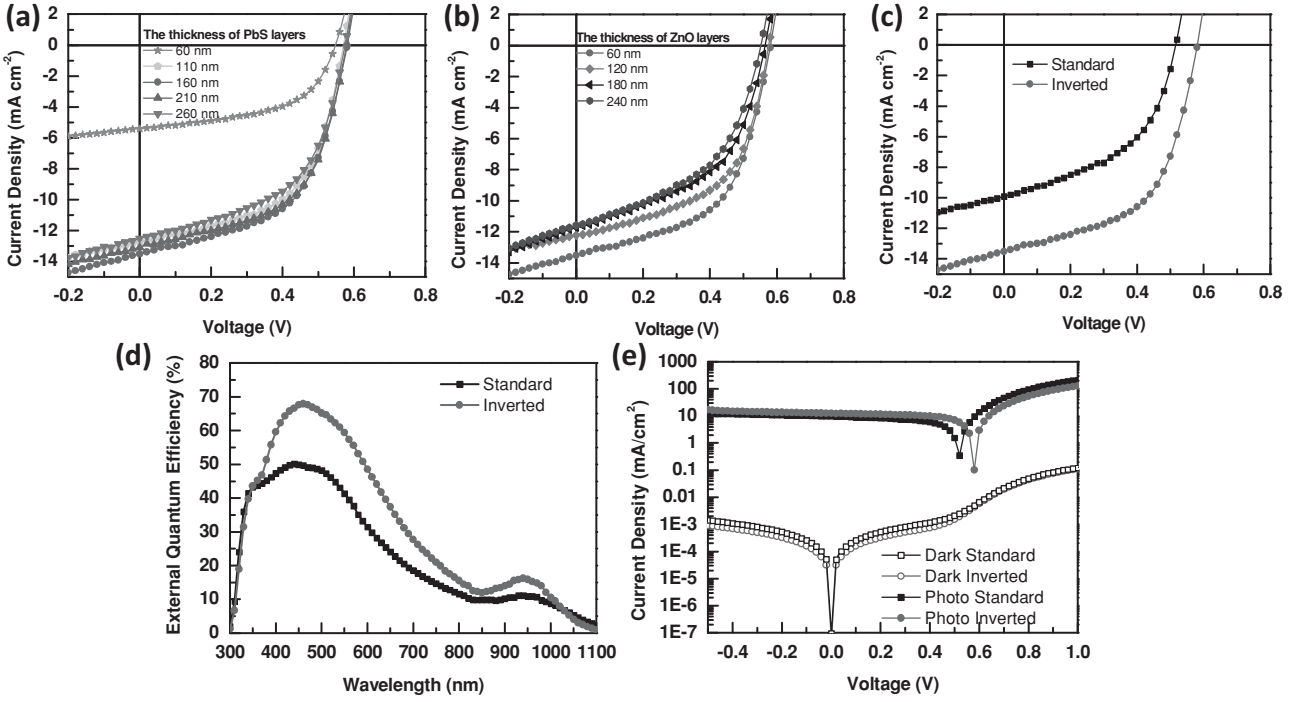

Figure 4. *J–V* characteristics of ITO/PEDOT:PSS/PbS/ZnO/Al devices with (a) variable PbS thickness, (b) variable ZnO thickness and (c) compared to ITO/ZnO/PbS/Au devices under 100 mW/cm^2 simulated solar irradiation. The external quantum efficiency of the optimized inverted and standard devices are reported in (d). *J–V* characteristics for the optimized standard and inverted devices are compared in the light and dark (e).

Adv. Mater. **2014**,
DOI: 10.1002/adma.201305583

Table 1. Average photovoltaic characteristics of devices using the inverted structure (ITO/PEDOT:PSS/PbS/ZnO/Al) with different PbS and ZnO thickness. Characteristics of the best devices are given in parentheses.

PbS thickness (nm)	ZnO thickness (nm)	J_{SC} (mA/cm^2)	V_{OC} (V)	*FF*	*PCE* (%)
60	60	4.85 (5.41)	0.55 (0.55)	0.52 (0.54)	1.42 (1.61)
110	60	11.4 (12.7)	0.57 (0.57)	0.55 (0.56)	3.95 (4.05)
160	60	12.9 (13.5)	0.58 (0.58)	0.55 (0.55)	4.21 (4.31)
210	60	12.3 (13.1)	0.58 (0.58)	0.54 (0.56)	4.13 (4.25)
260	60	11.2 (12.5)	0.57 (0.58)	0.52 (0.53)	3.69 (3.84)
160	120	11.2 (12.2)	0.57 (0.58)	0.52 (0.54)	3.74 (3.82)
160	180	11.2 (11.7)	0.57 (0.57)	0.48 (0.50)	3.05 (3.33)
160	240	10.5 (11.6)	0.54 (0.55)	0.46 (0.48)	2.85 (3.06)

Table 2. Average photovoltaic characteristics of devices using the standard structure (ITO/ZnO/PbS/Au) with different PbS and ZnO thickness. Characteristics of the best devices are given in parentheses.

PbS thickness (nm)	ZnO thickness (nm)	J_{SC} (mA/cm^2)	V_{OC} (V)	*FF*	*PCE* (%)
110	60	7.89 (8.55)	0.50 (0.50)	0.48 (0.50)	2.02 (2.14)
160	60	8.85 (9.91)	0.52 (0.52)	0.49 (0.48)	2.25 (2.47)
210	60	9.15 (9.68)	0.50 (0.50)	0.47 (0.49)	2.15 (2.37)
260	60	7.68 (8.03)	0.50 (0.52)	0.46 (0.47)	1.75 (1.96)
160	120	8.85 (9.13)	0.50 (0.50)	0.47 (0.49)	2.06 (2.24)
160	180	7.42 (7.73)	0.50 (0.52)	0.45 (0.47)	1.67 (1.89)
160	240	7.15 (7.70)	0.50 (0.50)	0.44 (0.46)	1.55 (1.77)

To verify that the enhancement in the J_{SC} arises from the optical spacer effect, we performed UV-Vis absorption measurements (**Figure 5**) in reflection mode. The total absorption by the CQD layer (including the doubled path length in the active layer as a result of reflection from the reflective metal electrode) with and without ZnO spacer are shown in Figure 5. Comparing two devices with the same active layer thickness, an enhancement in absorption across the solar spectrum is observed in the cell with the optical spacer.[16,19]

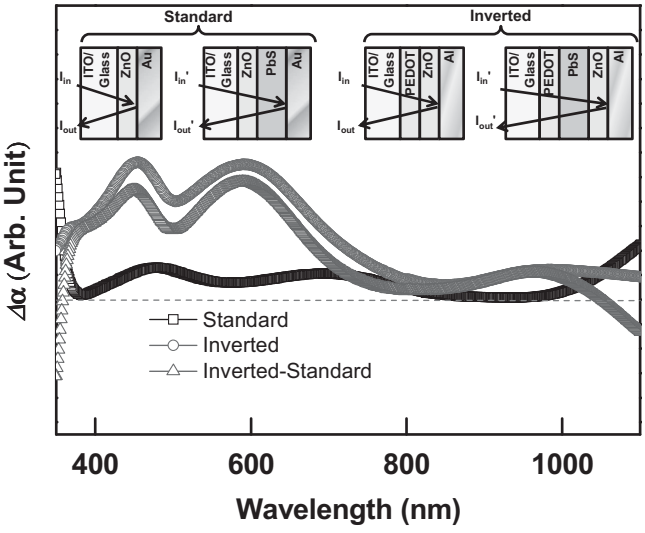

Figure 5. Change in the absorption spectrum ($\Delta\alpha(\Omega)$) due to the PbS CQD layer in inverted and standard architectures according to equation: $\Delta\alpha(\Omega) = -(1d/2)ln(I'_{out}(\Omega)/I_{out}(\Omega))$,[16] as well as the difference in $\Delta\alpha(\Omega)$ (inverted $\Delta\alpha(\Omega)$ – standard $\Delta\alpha(\Omega)$) between the two architectures. The inset is a schematic of the optical beam path in the samples.

Additionally, the enhanced absorption is in good agreement with external quantum efficiency (EQE) spectra (Figure 4d) in the spectral range of 300 nm to 1100 nm. The observed enhancement in EQE for the inverted structure occurs in the same region where enhanced light absorption ($\Delta\alpha(\Omega)$) is observed in reflectance measurements (see Figure 4d and Figure 5).[16] The EQE features closely match the absorption spectrum as shown in Figure S1. The calculated J_{SC} value of 13.8 mA/cm^2 obtained by integrating the EQE data is similar to the measured value of 13.5 mA/cm^2.

To probe further the detailed nature of light absorption enhancement in the PbS CQD layer using the inverted structure, we report the optical field ($|E|^2$) distribution throughout the devices (Figure S7) for a number of wavelengths of interest: 450, 700, and 950 nm, corresponding to the highest EQE value, the center of absorption, and the first excitonic transition peak of PbS, respectively. In the standard device architecture, $|E|^2$ drops to zero near the interface between the PbS CQD layer and the reflective Au electrode. This has the effect of pushing more integrated $|E|^2$ outside of the absorber, towards the front. In our inverted architecture, two peaks in $|E|^2$ occur in the PbS CQD active layer and the intensity is reduced in the ZnO layer whereas only one peak in $|E|^2$ appears within the PbS layer (at 950 nm) in the standard architecture. This enhanced $|E|^2$ distribution within the PbS layer causes an increased generation of charge carriers in the optimized cavity device.

However, although the calculated results indicate that increasing the PbS thickness up to ~500 nm continues to result in increasing photocurrent (see Figure S5), in practice, increasing the thickness of the PbS layer to more than 200 nm is not found to increase in the J_{SC}. As noted in the introduction, any materials employed for the enhancement of light absorption should not affect the carrier transport and extraction of the solar cell. Carrier extraction becomes increasingly inefficient in thick CQD films; these losses are not explicitly treated in the optical model. Although these transfer matrix calculations can only approximate upper limits to the photocurrent possible in a device and real photocurrents are perturbed by other losses, it is evident that when the thickness of the PbS CQD layer is limited to less than $1/\alpha$ it is possible to achieve enhanced absorption in the PbS layer via constructive optical interference. In particular, as the thickness of the PbS CQD layer increases, more photons are absorbed in the p-type PbS CQD layer; however, the photons absorbed too far from the PbS/ZnO interface do not contribute to photocurrent generation,[21] and we observe that the J_{SC} begins to decrease for PbS CQD thicknesses greater than about 200 nm. Small discrepancies may also arise from imperfect knowledge of the refractive index of PbS CQD films; a comparison of observed J_{SC} *vs.* predicted J_{SC} using different refractive index values can be found in supporting information (Figure S3). Increasing the ZnO layer thickness to 120, 180 and 240 nm results in a decrease in J_{SC}, from 12.7 to 12.2 to 11.7 to 11.6 mA/cm^2, generally following the trend modeled via the transfer matrix in which J_{SC} is predicted to decrease from 17.9 to 17.5 to 17.4 to 16.8 mA/cm^2.

While optical interference effects are predicted to increase the absorption and photocurrent generation in the inverted device considerably, interference effects alone may not account for the large observed increase in J_{SC} in the inverted architecture. Although we currently lack a complete understanding of the effect that diethyl zinc has on the electronic properties and structure of the PbS/ZnO junction, there are additional aspects which may contribute to improved device performance. Due to the small size of the diethyl zinc molecule (approximately 7 Å), it is possible that the diethyl zinc precursor is able to diffuse into the interstices in the PbS QD film, resulting in the formation of ZnO within the colloidal PbS CQD layer, thereby increasing the contact area between PbS CQD and ZnO phases and producing a form of bulk heterojunction. The device with the inverted structure shows a low R_S of 2.67 Ωcm^2 and a high R_{Sh} of 626 kΩ cm^2 compared to an R_S of 6.37 Ωcm^2 and R_{Sh} of 387 kΩ cm^2 with the standard structure. These improved diode characteristics may also contribute to an improved *FF* and *PCE*.

In summary, the effect of a ZnO optical cavity layer on inverted CQD solar cell devices has been investigated. The effect of device geometry on light absorption and overall photovoltaic performance was investigated using otherwise identical PbS CQD films. Optical modeling using a transfer matrix formalism has been utilized to explain performance variation in different device architectures. Optical interference after insertion of an optical cavity layer is shown to be responsible for significant differences observed in optical field distribution throughout the devices. Efficient inverted photovoltaic device structures were fabricated in which constructive interference occurs due to the optical cavity, resulting in improved photovoltaic device performance compared to optimal standard device geometry. By exploiting the ability of the transparent ZnO layer to function as an optical cavity in the inverted PbS/ZnO structure, CQD solar cells with a PCE of 4.3% have been demonstrated, which constitutes a significant improvement over the performance (2.5%) of the reference ZnO/PbS architecture made using the same active region and electron accepting materials.

Experimental Section

Synthesis: PbS nanoparticles were synthesized following a previous report[4] with small modification by adding lead oxide (PbO, 99.99%, Sigma-Aldrich) (0.47 g), oleic acid (OA, tech. grade 90%, Sigma-Aldrich) (2 g), and 1-octadecene (ODE, tech. grade 90%, Sigma-Aldrich) (10 g) to a three-neck round bottom flask. The mixture was heated to 125 °C under vacuum for 1 hr and then kept under argon. In a glove box, hexamethyldisilathiane (synthetic grade, Sigma-Aldrich, 180 µL) was mixed with ODE and loaded into a syringe. The contents of the syringe were quickly injected into the flask, the heating mantle was removed after 1 minute and the PbS nanoparticles were cooled to room temperature. The reacted solution was mixed with toluene (10 mL), ethanol (10 mL), and acetone (10 mL) and centrifuged to isolate the PbS nanoparticles. This washing step was repeated several times. The nanoparticles synthesized in this way have a diameter of about 3.7 nm, consistent with optical energy gap at 950 nm observed for the first absorption band (Figure S1).

Device Fabrication: Devices were fabricated using the following procedure: Clevios PH PEDOT:PSS purchased from H. C. Starck (Germany) was spin-coated on ITO coated glass substrates at 5000 rpm for 60 s and then baked at 140 °C for 10 min. PbS layers were then deposited by spin-coating a 10 mg ml^{-1} solution of CQDs in octane at 1500 rpm for 15s. The oleate ligands of the CQDs were exchanged by immersing the films into a solution of 10% (v/v) MPA in methanol for 1 minute, then sequentially rinsing with methanol and octane at 1500 rpm for 15 s in a modified version of a previously reported procedure.[4] PbS CQDs were spin-coated multiple times in this way to achieve PbS CQD films of variable thickness. The highest performance devices were obtained from PbS CQD films with a thickness of 160 nm, prepared by repeating the coating procedure 8 times. The ZnO layer was next deposited by diluting a diethylzinc solution[27] (Aldrich, 15 wt.% in toluene) with two parts tetrahydrofuran (note: the un-diluted diethyl zinc solution is highly reactive towards air and should be handled inside a glovebox; after dilution with THF, the solution becomes less reactive, however, appropriate safety precautions should be taken in case of an accidental spill or fire), filtering through a 0.45 µm PTFE syringe filter and spin coating at 3000 rpm for 30 s in air. The ZnO precursor solution was kept closed in a 4 mL vial while not in use and spin-coated by rapidly dispensing 25 µL onto an already spinning substrate using a micropipette with a plastic tip. The precursor solution forms solid ZnO on the pipette tip over time when exposed to air, therefore, a new plastic tip was used for each substrate to avoid the formation of large ZnO particulates. The ZnO layer was then annealed in air on a hot plate at 110 °C for 10 minutes, yielding a ZnO layer with a thickness of 60 nm. The PbS/ZnO device is stable up to 120 °C annealing, however, the performance dramatically decreases above 120 °C. Thicker ZnO films were prepared by repeating the spincoating and annealing steps. Finally, samples were transferred to a vacuum chamber (< 10^{-6} torr), and a 100 nm thick Al electrode was thermally evaporated on top of the ZnO layer through a shadow mask. The deposited Al electrode area defined the active area of the devices as 13 mm^2. Reported *J–V* characteristics reflect the average of between 10 and 20 devices.

Film Characterization: UV-Vis-NIR absorption and reflectance spectra were measured on a Varian Cary 5000 spectrophotometer. The cross-sectional image of device was measured using a JEM-2100F (Cs

Adv. Mater. **2014**,
DOI: 10.1002/adma.201305583

corrector) HR-TEM. EQE measurements were obtained by using a PV measurements OE system equipped with a Xenon arc lamp where monochromated light was chopped at a frequency of 100 Hz and photocurrent response detected with a lock-in amplifier and compared to a reference silicon photodiode. Photovoltaic device characteristics were measured inside a glove box using a high quality optical fiber to guide light from a xenon arc lamp. *J–V* characteristics of the devices were measured using a Keithley 2635A Source Measure unit. Light intensity was calibrated using an NREL certified standard silicon solar cell with a protective window containing KG5 filter glass. UPS measurements were carried out using a KRATOS AXIS Nova instrument following previously reported procedures.[22] He I hv = 21.22 eV was used as a light source and thermally evaporated Au substrates were used as a reference. Workfunctions (Φ) were calculated from the onset of the secondary edge (E_{SE}) using the equation $\Phi = 21.22 - E_{SE}$. Valence band edges were taken relative to an Au reference with known Fermi energy.[22] Measured E_g, E_{VB}, E_{CB} and E_F for each material were used to construct a band diagram for the PbS/ZnO junction using an abrupt junction approximation assuming constant doping concentrations of 2×10^{16} cm^{-3} and 1×10^{17} cm^{-3} for PbS and ZnO, respectively,[4,23] where the depletion width was corrected in order to match the observed saturation of photocurrent in the PbS CQD layer.

Optical Modeling: Optical constants of ITO, PEDOT:PSS and ZnO layers were calculated from ellipsometric data in the range of wavelengths from 370 to 1200 nm. Reflectance data for Al and Au were taken from the literature.[24,25] Ellipsometric data for PbS CQD films could not be accurately fit, therefore, real parts of refractive indices (n) for the PbS CQD layer were taken from known values for bulk PbS[26] and adjusted to reflect a composite structure consisting of close-packed PbS nanoparticles (74.048 volume%) following a linear relationship previously observed between volume fraction and n previously observed in PbS nanocomposite films. The imaginary part (k) was derived from the absorption coefficient (α) of PbS CQD films as described by Burkhard, et al.[18]

Supporting Information

Supporting Information (An absorption spectra, Atomic force microscope, optical constant, optical distribution, additional optical models and additional *J–V* characteristics of standard structure (ITO/ZnO/PbS/Au)) is available from the Wiley Online Library or from the author.

Acknowledgements

This research was supported by the year of 2010 research fund of the UNIST, BK21 Plus funded by the Ministry of Education, Korea (10Z20130011057), the National Research Foundation of Korea Grant (NRF-2013R1A2A2A01015342), and the International Cooperation of the Korea Institute of Energy Technology Evaluation and Planning (KETEP) grant funded by the Korea government Ministry of Knowledge Economy (2012T100100740).

Received: November 11, 2013
Revised: December 26, 2013
Published online:

[1] P. V. Kamat, *J. Phys. Chem. C* **2008**, *112*, 18737.
[2] M. A. Hines, G. D. Scholes, *Adv. Mater.* **2003**, *15*, 1844.
[3] S. A. McDonald, G. Konstantatos, S. Zhang, P. W. Cyr, E. J. D. Klem, L. Levina, E. H. Sargent, *Nat. Mater.* **2005**, *4*, 138.
[4] A. G. Pattantyus-Abraham, I. J. Kramer, A. R. Barkhouse, X. Wang, G. Konstantatos, R. Debnath, L. Levina, I. Raabe, M. K. Nazeeruddin, M. Grätzel, E. H. Sargent, *ACS Nano* **2010**, *4*, 3374.
[5] I. Gur, N. A. Fromer, M. L. Geier, A. P. Alivisatos, *Science* **2005**, *310*, 462.
[6] D. Zhitomirsky, M. Furukawa, J. Tang, P. Stadler, S. Hoogland, O. Voznyy, H. Liu, E. H. Sargent, *Adv. Mater.* **2012**, *24*, 6181.
[7] K. M. Noone, E. Strein, N. C. Anderson, P.-T. Wu, S. A. Jenekhe, D. S. Ginger, *Nano Lett.* **2010**, *10*, 2635.
[8] W. Shockley, H. J. Queisser, *J. Appl. Phys.* **1961**, *32*, 510.
[9] A. J. Nozik, *Physica E.* **2002**, *14*, 115.
[10] R. J. Ellingson, M. C. Beard, J. C. Johnson, P. R. Yu, O. I. Micic, A. J. Nozik, A. Shabaev, *Nano Lett.* **2005**, *5*, 865.
[11] O. E. Semonin, J. M. Luther, S. Choi, H.-Y. Chen, J. Gao, A. J. Nozik, M. C. Beard, *Science* **2011**, *334*, 1530.
[12] A. J. Nozik, *Annu. Rev. Phys. Chem.* **2001**, *52*, 193.
[13] J. Tang, K. W. Kemp, S. Hoogland, K. S. Jeong, H. Liu, L. Levina, M. Furukawa, X. Wang, R. Debnath, D. Cha, K. W. Chou, A. Fischer, A. Amassian, J. B. Asbury, E. H. Sargent, *Nat. Mater.* **2011**, *10*, 765.
[14] Z. Ning, Y. Ren, S. Hoogland, O. Voznyy, L. Levina, P. Stadler, X. Lan, D. Zhitomirsky, E. H. Sargent, *Adv. Mater.* **2012**, *24*, 6295.
[15] A. H. Ip, S. M. Thon, S. Hoogland, O. Voznyy, D. Zhitomirsky, R. Debnath, L. Levina, L. R. Rollny, G. H. Carey, A. Fischer, K. W. Kemp, I. J. Kramer, Z. Ning, A. J. Labelle, K. W. Chou, A. Amassian, E. H. Sargent, *Nat . Nanotechnol.* **2012**, *7*, 577.
[16] J. Y. Kim, S. H. Kim, H. H. Lee, K. Lee, W. L. Ma, X. Gong, A. J. Heeger, *Adv. Mater.* **2006**, *18*, 572.
[17] L. A. A. Pettersson, L. Roman, O. Inganas, *Appl. Phys. Lett.* **1999**, *86*, 487.
[18] G. F. Burkhard, E. T. Hoke, M. D. McGehee, *Adv. Mater.* **2010**, *22*, 3293.
[19] K. Lee, Y. Chang, J. Y. Kim, *Thin Solid Films* **2003**, *423*, 131.
[20] L. Martinez, M. Bernechea, F. P. G. de Arquer, G. Konstantatos, *Adv. Energy Mater.* **2011**, *1*, 1029.
[21] J. J. Choi, W. N. Wenger, R. S. Hoffman, Y.-F. Lim, J. Luria, J. Jasieniak, J. A. Marohn, T. Hanrath, *Adv. Mater.* **2011**, *23*, 3144.
[22] J. H. Seo, R. Yang, J. Z. Brzezinski, B. Walker, G. C. Bazan, T.-Q. Nguyen, *Adv. Mater.* **2009**, *21*, 1006.
[23] A. Janotti, C. G. V. de Walle, *Rep. Prog. Phys.* **2009**, *72*, 126501.
[24] D. Y. Smith, E. Shiles, M. Inokuti, In *Handbook of Optical Constants of Solids* (Ed: Edward D. Palik) Academic Press: Burlington, **1997**, pp. 369.
[25] D. W. Lynch, W. R. Hunter, In *Handbook of Optical Constants of Solids* (Ed: Edward D. Palik) Academic Press: Burlington, **1997**, pp. 275.
[26] G. Guizzetti, A. Borghesi, In *Handbook of Optical Constants of Solids* (Ed: Edward D. Palik) Academic Press: Burlington, **1997**, pp. 525.
[27] M. T. Lloyd, C. H. Peters, A. Garcia, I. V. Kauvar, J. J. Berry, M. O. Reese, M. D. McGehee, D. S. Ginley, D. C. Olson, *Sol. Energ. Mat. Sol. Cells* **2011**, *95*, 1382.